

Article

Laser-Induced Magnetization Dynamics in Si-Doped Yttrium-Iron Garnet Film

Mikhail Gaponov , Sergey Ovcharenko , Nikita Ilyin and Elena Mishina *

Laboratory of Ultrafast Dynamics of Ferroics, MIREA—Russian Technological University, Moscow 119454, Russia

* Correspondence: mikhail.lab109@gmail.com (M.G.); mishina_elena57@mail.ru (E.M.)

Abstract: We experimentally demonstrate that the excitation of a silicon-doped yttrium-iron garnet film by femtosecond laser pulses triggers a magnetization precession with an amplitude determined by the external magnetization direction. The maximum efficiency is achieved at the pump wavelength corresponding to the absorption maximum due to doping with silicon ions. Based on the azimuthal dependences of the precession amplitude and frequency, it is shown that the magnetization dynamics is induced by a thermal disruption of the magnetocrystalline anisotropy. By modeling hysteresis loops, it was found that the silicon doping leads to a decrease in the value of the exchange interaction in the film and an increase in the anisotropy field.

Keywords: laser-induced magnetization dynamics; spintronics; domain structure; optical control of magnetization; pump-probe



Citation: Gaponov, M.; Ovcharenko, S.; Ilyin, N.; Mishina, E. Laser-Induced Magnetization Dynamics in Si-Doped Yttrium-Iron Garnet Film. *Condens. Matter* **2022**, *7*, 55. <https://doi.org/10.3390/condmat7040055>

Academic Editor: Annette Bussmann-Holder

Received: 1 August 2022

Accepted: 30 September 2022

Published: 8 October 2022

Publisher's Note: MDPI stays neutral with regard to jurisdictional claims in published maps and institutional affiliations.



Copyright: © 2022 by the authors. Licensee MDPI, Basel, Switzerland. This article is an open access article distributed under the terms and conditions of the Creative Commons Attribution (CC BY) license (<https://creativecommons.org/licenses/by/4.0/>).

1. Introduction

With the development of the field of ultrafast magnetism initiated in Ref. [1], the concepts of the optical control of magnetization by femtosecond laser pulses have significantly expanded [2,3]. As a result of the interaction of ultrashort laser pulses with magnetic matter, record speeds of magnetization switching at minimal energy consumption are achieved [4]. Moreover, the industry already produces opto-magnetic devices that use the effects of such interaction: Heat Assisted Magnetic Recording and Heated-dot magnetic recording [5], which, in turn, stimulates further research in this area [6,7].

The possibility of all-optical control of the magnetization by femtosecond laser irradiation has now been experimentally demonstrated on various classes of materials: metal films [8,9], dielectrics [10], semiconductors, and heterostructures [11]. Of particular relevance is the study of ultrafast optical control of magnetization in dielectrics with negligible absorption in the near-infrared spectral range, which are used for fiber-optic communication systems. Yttrium iron garnet (YIG) films have low absorption in this range and exhibit a strong magneto-optical interaction [12]. Optical control of magnetization on a femtosecond time scale in YIG films was demonstrated due to the inverse magneto-optical Faraday effect [13], photoinduced changes in magnetocrystalline anisotropy [14] and due to photoinduced phonon to magnon conversion [15].

Even more effective magnetization control can be expected due to substitution of Fe²⁺ ions, which is characterized by a strong contribution to single ion magnetic anisotropy [16]. For example, ultrafast all-optical switching at room temperature with unprecedented low thermal loss was shown in Co-doped YIG film [17]. On the other hand, Si-doped YIG has been proposed for optical recording decades ago. The effect was observed when recording with a CW-laser irradiation at low temperatures and is based on the inverse magneto-optical effect, since the dependence of the recording efficiency on the polarization orientation was observed. It has been shown that ferrous iron introduced by substitution with a tetravalent ion, such as Si, Ge, and Sn, affects the absorption in the visible range. At low temperatures, such films are characterized by photoinduced anisotropy and dichroism [18]. Thus, the presence of Si impurities in YIG films can have a significant effect on the

dynamics of magnetization on a femtosecond time scale at room temperature and requires a detailed analysis.

In this paper, we focus on the ultrafast photoexcitation of magnetization by femtosecond laser pulses in a Si-doped YIG film at room temperature.

2. Materials and Methods

A Si doped YIG sample was fabricated by liquid-phase epitaxy on a (111) gallium gadolinium garnet (GGG) substrate. The content of silicon is 0.3 formula units, the film thickness is 4.8 μm .

The magnetic properties of the film were determined using the magneto-optical Faraday effect and MOKE imaging with in-plane magnetization. According to the YIG crystallographic symmetry, the influence of cubic anisotropy was expected, and the sample was installed with the possibility to change orientation of the $[\bar{1}11]$ axis projection on the film plane relative to the X-axis of the laboratory frame, determined by the angle φ (Figure 1a).

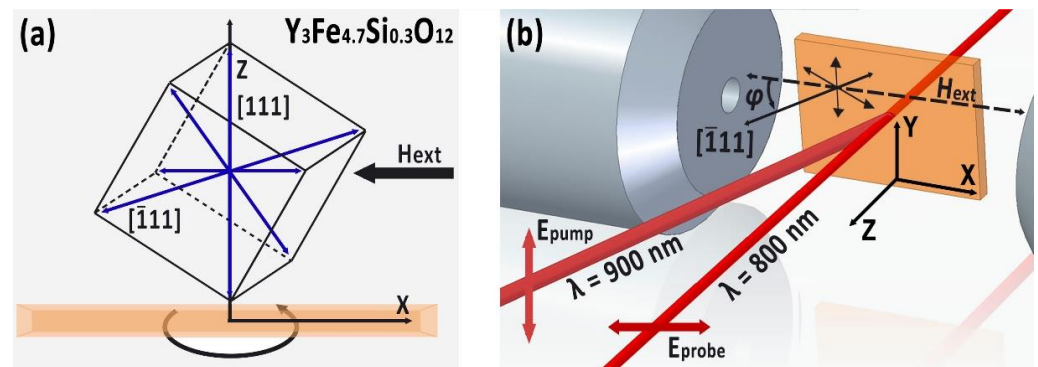


Figure 1. (a) Schematic of the crystallographic orientation of the sample. In blue—orientation of crystallographic anisotropy axes. The sample rotated around the $[111]$ axis. (b) Geometry of the pump-probe setup. XYZ-laboratory frame.

2.1. Dynamic Conditions:

The magnetization dynamics was studied by time-resolved spectroscopy [13] in the time range up to 300 ps based on the magneto-optical Faraday effect, corresponding to the out of plane magnetization component M_z . Experimental setup is shown in Figure 1b. The femtosecond laser system («Avesta-project», Russia) was used, consisting of a Ti:Sapphire femtosecond laser with a regenerative amplifier and an optical parametric amplifier (OPA). The laser system provides a pulse of wavelength $\lambda = 800$ nm at a repetition rate of 3 kHz with a duration of 35 fs. Small part of the laser radiation at 800 nm was used as probe. The rest was directed to OPA which provided the pump wavelength in the range from 880 nm up to 1020 nm. Both pump and probe beams were focused and spatially overlapped on the sample with the spot diameter of 190 μm and 170 μm and power density of 3.5 mJ/cm^2 and 0.1 mJ/cm^2 , respectively. Angle of incidence for pump beam is 20 degrees, and probe incident along the normal.

The probe and pump radiation were linearly polarized. The polarization plane of the probe radiation was parallel to the X-axis and the applied external magnetic field (p-polarization), and for the pumping radiation, the radiation polarization plane orthogonal to the probe (s-polarization).

A balanced photodetector allowed to simultaneously record the change in the reflection intensity and the angle of the polarization rotation. In order to increase the signal-to-noise ratio the signal was recorded by synchronous amplifier (Lock-in amplifier SR830, Stanford Research Systems). The sample was placed between the cores of an electromagnet providing a DC magnetic field up to 650 mT in the gap.

2.2. Static Conditions

Hysteresis loops at different azimuthal positions were measured using the same set-up with the pump beam blocked. The corresponding domain structure was obtained by a home-made confocal MOKE microscope for the sample preliminary magnetized by an in-plane H of 3 kOe for the same azimuthal position of the sample.

3. Results and Discussion

3.1. Static Conditions

Figure 2c,d shows corresponding images of domain structures. These two types of loops and domain structures repeat every 60 degrees. For 0 degrees azimuth, the loop consists of three subloops in the field ranges $\pm 1.5 \div \pm 0.5$ kOe, and $-0.5 \div 0.5$ kOe. For higher fields magnetization amplitude decreases and almost reaches saturation. Residual magnetization forms bubble domains. At 30 degrees, the hysteresis loop is very narrow with the maximum of magnetization around 0.8 kOe. Saturation magnetization is almost coincident with that at zero degrees azimuth. Residual magnetization forms labyrinth domain structure.

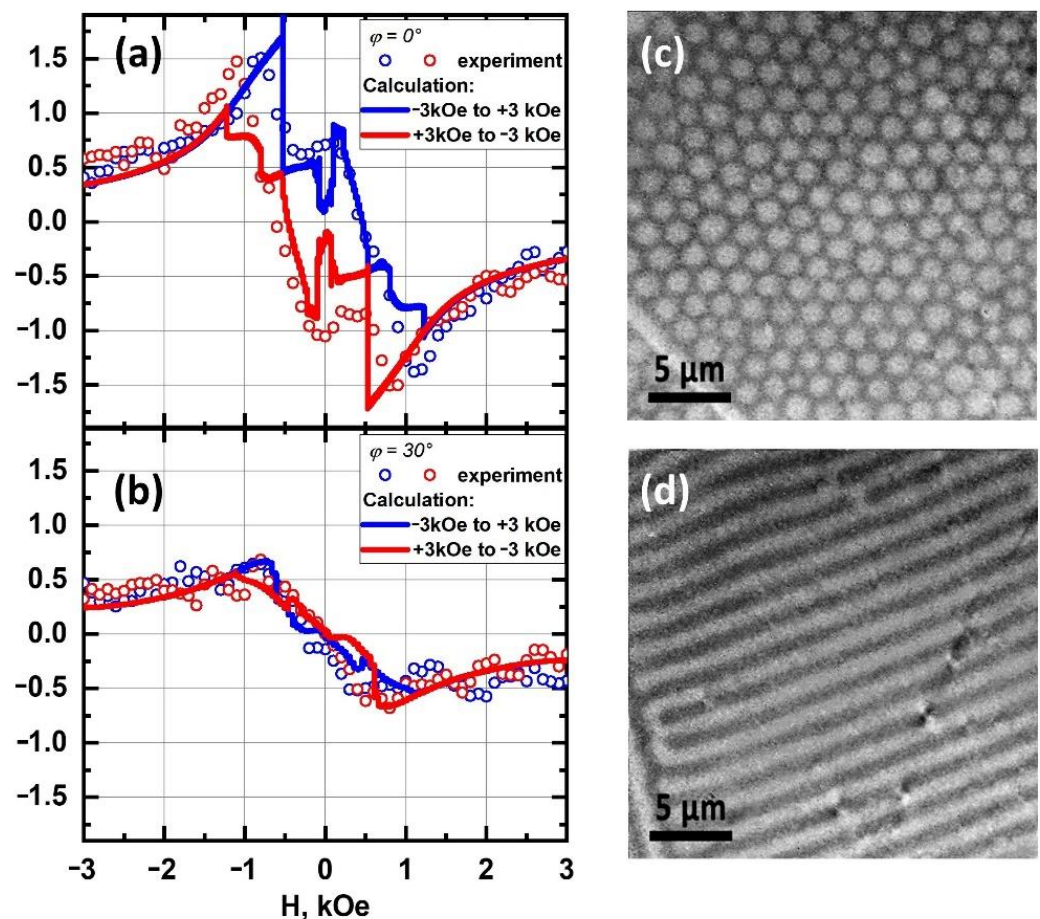


Figure 2. Static conditions. (a,b)—experimentally obtained (red dots) and calculated (solid lines) Faraday rotation angle hysteresis with in-plane magnetization for the azimuthal position φ of the sample of 0 and 30 degrees, respectively; $\varphi = 0$ corresponds to the coincidence of the projection of the axis $[\bar{1}11]$ with the laboratory x axis (c,d)—MOKE images of the domain structure upon preliminary magnetization by an in-plane H of 3 kOe $\varphi = 0$ and $\varphi = 30$ degrees, respectively.

The observed static picture with the period of 60 degrees points to the strong cubic anisotropy since the magnetic field H changes its direction from the easy axis to the hard one

every 30 degrees. Although slight in-plane magnetic anisotropy also can exist analogously to [19].

To estimate the contribution of doping yttrium iron garnet with tetravalent silicon, we calculated the magnetic hysteresis loop in the software package for three-dimensional micromagnetic modeling OOMMF [20], based on the Landau–Lifshitz–Gilbert formalism for the motion of the magnetic moment:

$$\frac{\partial M}{\partial t} = -\gamma \left[M \times H_{eff} \right] + \frac{\alpha}{M_s} \left[M \times \frac{\partial M}{\partial t} \right], \quad (1)$$

where M_s is the saturation magnetization, H_{eff} is the effective magnetic field determined taking into account the exchange interaction A , cubic anisotropy, the demagnetizing and applied external field H , is the gyromagnetic ratio, and α is the Gilbert damping coefficient. The calculation of the hysteresis loop was carried out by searching for the minimum energy of a magnet under given external conditions. In this case, the Gilbert damping value is fixed at $\alpha = 0.5$ and does not affect the final result. The calculation uses $3N$ —the dimensional space of possible magnetization configurations, where N is the number of spins in the simulation. Once a minimum is found along a given direction, a new direction is chosen that is orthogonal to all previous directions, but related to the energy gradient taken relative to the magnetization. The area for calculation was a cube, with the $100 \times 100 \times 100 \text{ nm}^3$. The unit cell size was 5 nm. Cubic anisotropy with the directions [111] and [0–11] relative to the laboratory coordinate system, respectively, was specified in the calculation. The third anisotropy axis is computed as the vector product. The anisotropy energy density for cell i is given by

$$E_i = \frac{1}{2} \mu_0 M_s H_i \left(l_1^2 l_2^2 + l_2^2 l_3^2 + l_3^2 l_1^2 \right), \quad (2)$$

where $l_1 = m \times u_1$, $l_2 = m \times u_2$, $l_3 = m \times u_3$, for reduced (normalized) magnetization m and orthonormal anisotropy axes u_1 , u_2 , and u_3 at cell i . M_s is the saturation magnetization in cell i . H_i is the anisotropy field in cell i . For each cell, the axis directions are easy axes if H_i is >0 , or hard axes if H_i is <0 .

The direction of the external field H is set in the film plane in the range from -3 kOe to $+3 \text{ kOe}$ with a step of 50 Oe . Figure 2a,b shows by lines the calculated hysteresis loop for the studied sample, which repeats the experimental data. The best proximity to the experimental results was obtained while simulation was carried out with the following parameters: saturation magnetization $M_s = 2.8 \times 10^5 \text{ A/m}$, Anisotropy field $H_A = 6.5 \times 10^4 \text{ A/m}$ and exchange interaction value $A = 1.3 \times 10^{-12} \text{ J/m}$. For pure YIG, these values are usually considered as follows: $M_s = (0.16 \div 4) \times 10^5 \text{ A/m}$, anisotropy field $H_A = 0.2 \times 10^3 \text{ A/m}$ and the value of the exchange interaction $A = 4 \times 10^{-12} \text{ J/m}$ [21]. Thus, in the Si-doped YIG we observed an increase of the anisotropy field and a decrease in the value of the exchange interaction, which can be associated with a change in the symmetry of the crystal upon doping.

3.2. Dynamic Conditions

Figure 3a shows the dependence of pump-induced Faraday rotation angle related to the azimuthal position of the sample in a DC in-plane magnetic field $H = 3 \text{ kOe}$. It is important that DC magnetic field at which the measurements were carried out exceeds the H_A for this sample, since changing the magnetic domain structure from one type to another by changing the azimuth position was possible only after the sample was magnetically saturated. To study the excitation efficiency of the magnetization precession, the spectral dependence of the amplitude of the photoexcited magnetic moment deviation on the pump wavelength in the range of $880\text{--}1020 \text{ nm}$ was measured (Figure 3b) in a DC in-plane magnetic field of 3 kOe along the projection of the hard axis onto the plane of the

sample. Further, the obtained pump-induced Faraday rotation were approximated by a phenomenological dependence [22]:

$$\Delta\theta_F = I_1 \cdot \sin(2\pi\nu\Delta t + \varphi_0) \cdot \exp\left(-\frac{x}{\tau_1}\right) + I_2 \cdot \exp\left(-\frac{x}{\tau_2}\right), \quad (3)$$

where ν and φ_0 —spin precession frequency and phase; τ_1 —magnetization precession decay time; τ_2 —relaxation time of the magnetization, I_1, I_2 —amplitudes, which characterize the precessional motion and thermal relaxation respectively. In this way, we obtained the values of the precession frequencies ν , phases φ_0 , and amplitudes for the different wavelength and different azimuthal angles.

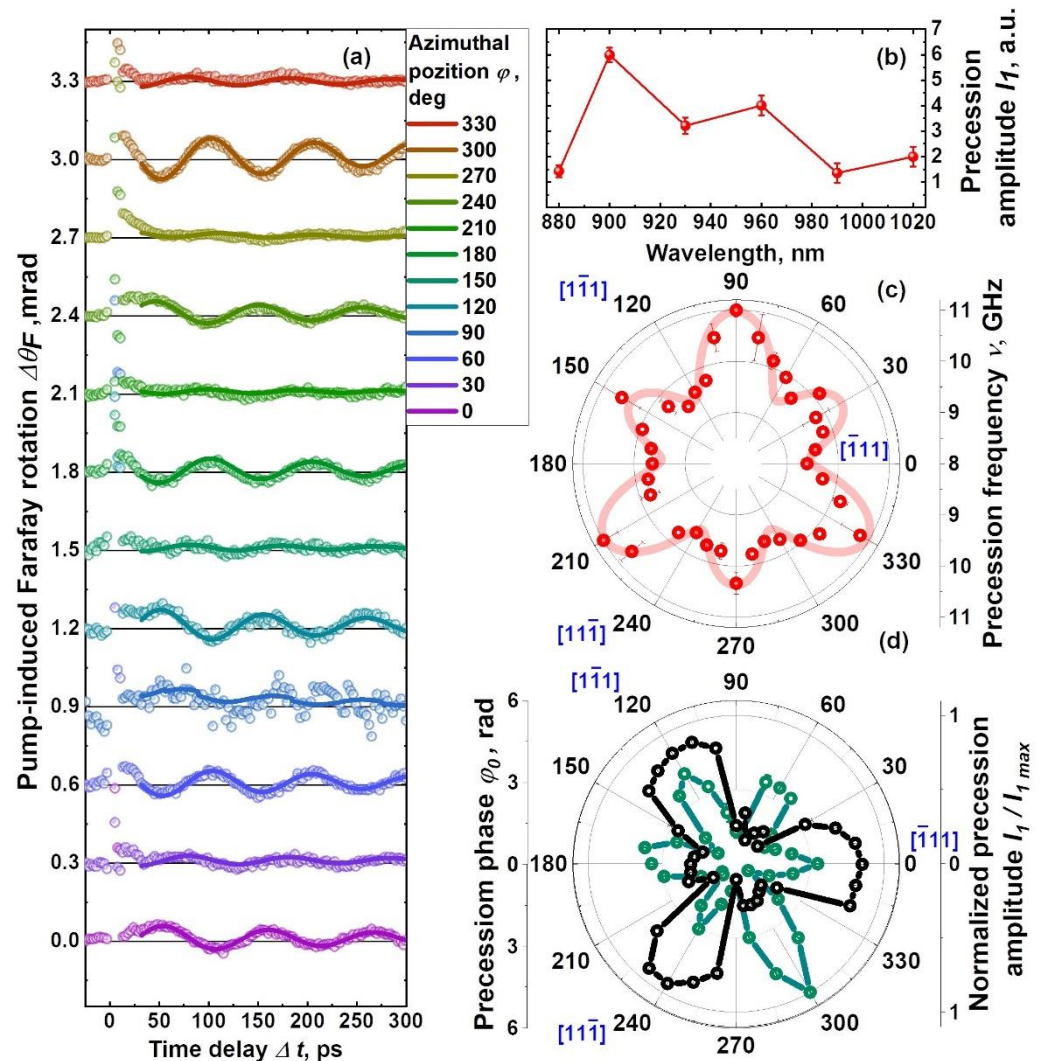


Figure 3. (a) Pump-induced Faraday rotation $\Delta\theta_F$ on the delay time for different azimuthal orientations φ of the sample at a magnetic field $H = 3$ kOe (the graphs are presented with an offset). Symbols represent the experimental data points, and the solid line is the best fit to the data; (b) spectral dependence of the magnetization precession amplitude I_1 for various pump wavelengths (line is guide for eye); (c) dependence of the experimental (dot) and calculated (line) precession frequency ν on the azimuthal position of the sample φ . (d) Dependence of the laser-induced normalized modulus of the spin precession amplitude $|I/I_{max}|$ (in green) and phase φ_0 (in black) on the azimuthal position of the sample φ obtained from fit. Lines are guide for eye.

In the spectral dependence of the precession amplitude, the maximum was found at 900 nm. Compare now these data for doped YIG with those for pure YIG. For pure YIG, in the wavelength range of 900–950 nm, there is a local absorption peak associated with spin

and parity-“forbidden” d-d transitions in the Fe³⁺ ions and a tail from higher energy charge transfer transitions at 2.8 and 3.4 eV [21]. When doped with silicon, tetravalent silicon ions replace iron ions in tetrahedral positions, lowering the symmetry of the octahedral positions of iron ions surrounding the silicon ion. In addition, to fulfill the conditions of electrical neutrality, the corresponding number of iron ions in octahedral sites must be divalent. It is these changes in the crystal lattice of YIG doped with silicon that cause an increase in absorption (at a Si⁴⁺ ion concentration of more than 0.1 formula unit), as well as the phenomena of photoinduced anisotropy and photoinduced dichroism [23]. However, in our experiment, the observed effect is laser-induced, and the peak of the photoinduced response can only be associated with an absorption increase due to silicon.

Consider now the precession parameters. In the case of cubic anisotropy, when the orientation of the magnetic field *H* relative to the hard axes changes, which occurs with each rotation of the sample through an angle $\Delta\phi$, a change in the precession frequency should be observed, provided that the field strength *H* is fixed. From the azimuth dependence of the frequency (Figure 3c), three maxima can be distinguished with a frequency of about 11 GHz, repeating every 120 degrees. Offset by 60 degrees, there are three maxima at a lower frequency, around 10.5 GHz. This dependence is specific for pure YIG films with the [111] orientation and was observed earlier in the study of the frequency and orientation characteristics of the propagation of magnetostatic waves [24]. The reason for the difference in frequency, for example, at 60 and 240 (0 and 180, etc.) degrees is determined by a slight inclination of the magnetic field *H* from the sample plane. Using the magnetic parameters obtained in the calculation of hysteresis loops, the frequency of laser-induced ferromagnetic resonance was calculated based on following equation [25,26]:

$$\frac{\nu}{\gamma} = \frac{1}{M_s \sin \theta} \sqrt{\frac{d^2F}{d\theta^2} \frac{d^2F}{d\phi^2} - \frac{d^2F}{d\theta d\phi}}, \tag{4}$$

where ν is the angular frequency, γ is gyromagnetic ratio, θ and ϕ are polar and azimuthal magnetization angles, respectively. The energy of the ferromagnet *F* was determined during the calculation as the sum of the external field energy *H* (Zeeman energy), the energy of the demagnetizing field (magnetostatic energy), and the energy of cubic magnetic anisotropy:

$$F = -\frac{1}{2}MH + 2\pi M_z^2 + K_1 (l_1^2 l_2^2 + l_2^2 l_3^2 + l_3^2 l_1^2), \tag{5}$$

where K_1 is the cubic anisotropy constant. The results of the calculation providing the convergence with the frequency values obtained from the fitting are shown in Figure 3c. The anisotropy constant K_1 was 7×10^3 J/m³. It follows from the calculation that the frequency maxima correspond to magnetization along the projections of the easy axes of cubic anisotropy onto the plane of the sample. The inclination of the field *H* relative to the plane of the sample, required for the corresponding asymmetry of the ν azimuthal dependence, is about 2 degrees.

The maximum (Figure 3d) of normalized spin precession amplitude modulus $|I_1/I_{max}|$ is obtained at 6 azimuth positions of the sample with a step of 60 degrees. The amplitude maxima coincide with the frequency minima, which is typical for laser-induced ferromagnetic resonance (FMR) [27,28]. The asymmetry of the amplitudes at the maxima can be associated with the presence of growth-induced uniaxial anisotropy. The damping constant τ_1 was 300 ps, and no noticeable dependence of these parameters on the azimuthal position was found. This parameter is related to precession damping (Gilbert damping) and depends on the magnetic properties of a particular sample [29]. The precession phase ϕ_0 has three “maxima” every 120 degree (Figure 3d), which corresponds to magnetization along symmetrically located projections of oppositely directed hard axes of magnetocrystalline anisotropy.

We assume that we observe an effect associated with the heating of the sample. The main argument in favor of photoinduced effects is the dependence of the excitation on the

polarization orientation of the pump radiation. For our sample, the result of the excitation of the magnetization dynamics does not depend on the orientation of the pump linear polarization. Another argument is an increase in the amplitude of the magnetization precession induced by the laser pulse with an increase in the energy density. Amplitude I_1 reflects the efficiency of excitation of precisely laser-induced FMR in the totality of the observed effects (laser-induced dynamics of magnetization, thermalization, cooling of the electronic subsystem). It is a component of the laser-induced Faraday rotation, associated with the precessional motion of the magnetic moment, which is generally determined by the LLG equation [30]. According to this theory, precession in the case of cubic anisotropy can be caused either by a change in the magnitude of the cubic anisotropy field H_A or in the demagnetization field. Since the demagnetization field $4\pi M_s = 1130$ G is much smaller than the anisotropy field H_A in this sample, it is the anisotropy field that makes the greatest contribution in laser-induced precession. A similar process was observed by us earlier, for example, in magnetic multilayer structures with strong TbCo₂/FeCo anisotropy [31].

4. Conclusions

When studying magnetization dynamics with a pumping wavelength of 900 nm, corresponding to the transition energy of the Fe²⁺ ion, the azimuthal dependence of the spin precession excitation efficiency was obtained at room temperature. The maximum efficiency is observed when the field is applied along the projection of the hard axis of cubic magnetic anisotropy onto the film plane. A similar dependence was already observed at slower times in [24], where the dependence of the FMR frequency on sample orientation in an external field was demonstrated, but the change in the FMR frequency was only about 0.3 percent of the absolute value.

According to the simulation of the hysteresis loop, the doping of YIG with silicon ions at a concentration of 0.3 formula units led to a decrease in the value of the exchange interaction and an increase in the anisotropy field can be associated with a change in the symmetry of the crystal upon doping. Previously, laser-induced control of the magnetization in this material was observed only at low temperatures. Thus, doping with silicon ions leads to a decrease in the value of the exchange interaction of the YIG film and an increase in the anisotropy field, but also increases absorption at a wavelength of about 900 nm and makes it possible to increase the efficiency of magnetization control due to ultrafast laser-induced heating at room temperature.

Author Contributions: Conceptualization, E.M.; methodology, N.I.; validation, E.M. and S.O.; formal analysis, S.O. and M.G.; investigation, S.O. and M.G.; writing—original draft preparation, M.G, S.O., and E.M.; writing—review and editing, E.M.; visualization, S.O. and M.G.; supervision, E.M.; project administration, E.M.; funding acquisition, E.M. All authors have read and agreed to the published version of the manuscript.

Funding: This work was supported by the Russian Foundation for Basic Research (grant NO 20-32-90206 “Postgraduate students”), by RTU MIREA (grant NICH-50 “For young scientists”), and by the Ministry of Education and Science of the Russian Federation (Grant No. 075-15-2022-1131). The work was partially carried out using the equipment of the joint educational and scientific center for collective use of RTU MIREA, supported from the Ministry of Science and Higher Education of the Russian Federation under Agreement No. 075-15-2021-689 dated 1 September 2021.

Institutional Review Board Statement: Not applicable.

Informed Consent Statement: Not applicable.

Data Availability Statement: Not applicable.

Acknowledgments: The authors express their gratitude to M.V. Logunov for sample preparing, A. Kimel and V.L. Preobrazhensky for useful discussions.

Conflicts of Interest: The authors declare no conflict of interest.

References

1. Beaupaire, E.; Merle, J.C.; Daunois, A.; Bigot, J.Y. Ultrafast spin dynamics in ferromagnetic nickel. *Phys. Rev. Lett.* **1996**, *76*, 4250. [[CrossRef](#)] [[PubMed](#)]
2. Kimel, A.V.; Kalashnikova, A.M.; Pogrebna, A.; Zvezdin, A.K. Fundamentals and perspectives of ultrafast photoferroic recording. *Phys. Rep.* **2020**, *852*, 1–46. [[CrossRef](#)]
3. Vedmedenko, E.Y.; Kawakami, R.K.; Sheka, D.D.; Gambardella, P.; Kirilyuk, A.; Hirohata, A.; Binek, C.; Chubykalo-Fesenko, O.; Sanvito, S.; Kirby, B.J.; et al. The 2020 magnetism roadmap. *J. Phys. D: Appl. Phys.* **2020**, *53*, 453001. [[CrossRef](#)]
4. Kimel, A.V.; Li, M. Writing magnetic memory with ultrashort light pulses. *Nat. Rev. Mater.* **2019**, *4*, 189–200. [[CrossRef](#)]
5. HAMR: The Next Leap Forward is Now. Available online: <https://blog.seagate.com/craftsman-ship/hamr-next-leap-forward-now/> (accessed on 29 September 2022).
6. Akagi, F.; Sakamoto, Y.; Matsushima, N. Effects of Static Magnetic Fields and Temperature Increase on 3D Magnetic Storage in Heated-Dot Magnetic Recording (Revised May 2021). In Proceedings of the 2021 IEEE International Magnetic Conference (INTERMAG), Lyon, France, 26–30 April 2021; pp. 1–5.
7. Mohan, J.R.; Medwal, R.; Gupta, S.; Gogia, K.; Vas, J.V.; Gupta, R.; Deka, A.; Rawat, R.S.; Subramanian, A.; Fukuma, Y. Nonstoichiometric FePt Nanoclusters for Heated Dot Magnetic Recording Media. *ACS Appl. Nano Mater.* **2021**, *4*, 7079–7085. [[CrossRef](#)]
8. Stanciu, C.D.; Hansteen, F.; Kimel, A.V.; Kirilyuk, A.; Tsukamoto, A.; Itoh, A.; Rasing, T. All-Optical Magnetic Recording with Circularly Polarized Light. *Phys. Rev. Lett.* **2007**, *99*, 047601. [[CrossRef](#)] [[PubMed](#)]
9. Ovcharenko, S.V.; Yakushenkov, P.O.; Ilyin, N.A.; Brekhov, K.A.; Semenova, E.M.; Wu, A.; Mishina, E.D. Ultrafast Magnetization Reversal in DyFeCo Thin Film by Single Femtosecond Laser Pulse. *Phys. Met. Metallogr.* **2019**, *120*, 825–830. [[CrossRef](#)]
10. Stupakiewicz, A.; Szerenos, K.; Afanasiev, D.; Kirilyuk, A.; Kimel, A.V. Ultrafast nonthermal photo-magnetic recording in a transparent medium. *Nature* **2017**, *542*, 71–74. [[CrossRef](#)] [[PubMed](#)]
11. Mangin, S.; Gottwald, M.; Lambert, C.-H.; Steil, D.; Uhlř, V.; Pang, L.; Hehn, M.; Alebrand, S.; Cinchetti, M.; Malinowski, G.; et al. Engineered materials for all-optical helicity-dependent magnetic switching. *Nat. Mater.* **2014**, *13*, 286–292. [[CrossRef](#)]
12. Zvezdin, A.K.; Kotov, V.A. *Magneto-Optics of Thin Films*; Nauka: Moscow, Ruassia, 1988.
13. Hansteen, F.; Kimel, A.; Kirilyuk, A.; Rasing, T. Nonthermal ultrafast optical control of the magnetization in garnet films. *Phys. Rev. B* **2006**, *73*, 014421. [[CrossRef](#)]
14. Davies, C.S.; Prabhakara, K.H.; Davydova, M.D.; Zvezdin, K.A.; Shapaeva, T.B.; Wang, S.; Zvezdin, A.K.; Kirilyuk, A.; Rasing, T.; Kimel, A.V. Anomalous Damped Heat-Assisted Route for Precessional Magnetization Reversal in an Iron Garnet. *Phys. Rev. Lett.* **2019**, *122*, 027202. [[CrossRef](#)] [[PubMed](#)]
15. Stupakiewicz, A.; Davies, C.S.; Szerenos, K.; Afanasiev, D.; Rabinovich, K.S.; Boris, A.V.; Caviglia, A.; Kimel, A.V.; Kirilyuk, A. Ultrafast phononic switching of magnetization. *Nat. Phys.* **2021**, *17*, 489–492. [[CrossRef](#)]
16. Stupakiewicz, A.; Szerenos, K.; Davydova, M.D.; Zvezdin, K.A.; Zvezdin, A.K.; Kirilyuk, A.; Kimel, A.V. Selection rules for all-optical magnetic recording in iron garnet. *Nat. Commun.* **2019**, *10*, 612. [[CrossRef](#)] [[PubMed](#)]
17. Szerenos, K.; Kimel, A.V.; Maziewski, A.; Kirilyuk, A.; Stupakiewicz, A. Fundamental Limits on the Repetition Rate of Photomagnetic Recording. *Phys. Rev. Appl.* **2019**, *12*, 044057. [[CrossRef](#)]
18. Wood, D.L.; Remeika, J.P. Effect of Impurities on the Optical Properties of Yttrium Iron Garnet. *J. Appl. Phys.* **1967**, *38*, 1038–1045. [[CrossRef](#)]
19. McGlashan-Powell, M.; Wolfe, R.; Dillon, J.F.; Fratello, V.J. Magneto-optic waveguide hysteresis loops of “planar” magnetic garnet films. *J. Appl. Phys.* **1989**, *66*, 3342–3347. [[CrossRef](#)]
20. Donahue, M.J.; Porter, D.G. *OOMMF User’s Guide, Version 1.0*; National Institute of Standards and Technology: Gaithersburg, MD, USA, 1999.
21. Newnham, R. Magnetic garnets. *Mater. Res. Bull.* **1981**, *16*, 1473–1474. [[CrossRef](#)]
22. Ovcharenko, S.V.; Gaponov, M.S.; Ilyin, N.A.; Logunov, M.V.; Wu, A.; Mishina, E.D. Laser-induced spin dynamics in the iron-yttrium garnet film doped with Si ions. *Russ. Technol. J.* **2020**, *8*, 58–66. [[CrossRef](#)]
23. Dillon, J.F.; Gyorgy, E.M.; Remeika, J.P. Photoinduced Uniaxial Magnetic Anisotropy and Optical Dichroism in Silicon-Doped Yttrium Iron Garnet [YIG(Si)]. *J. Appl. Phys.* **1970**, *41*, 1211–1217. [[CrossRef](#)]
24. Vashkovskii, A.V.; Lokk, Ę.G.; Shcheglov, V.I. Influence of induced uniaxial anisotropy on the domain structure and phase transitions of yttrium-iron garnet films. *Phys. Solid State* **1999**, *41*, 1868–1874. [[CrossRef](#)]
25. Vonsovskii, S.V. *Ferromagnetic Resonance*; Elsevier, Pergamon Press: Oxford, UK, 1966; ISBN 9780080110271. Available online: <https://www.elsevier.com/books/ferromagnetic-resonance/vonsovskii/978-0-08-011027-1> (accessed on 29 September 2022).
26. Makino, H.; Hidaka, Y. Determination of magnetic anisotropy constants for bubble garnet epitaxial films using field orientation dependence in ferromagnetic resonances. *Mater. Res. Bull.* **1981**, *16*, 957–966. [[CrossRef](#)]
27. Ma, T.P.; Zhang, S.F.; Yang, Y.; Chen, Z.H.; Zhao, H.B.; Wu, Y.Z. Distinguishing the laser-induced spin precession excitation mechanism in Fe/MgO(001) through field orientation dependent measurements. *J. Appl. Phys.* **2015**, *117*, 013903. [[CrossRef](#)]
28. Khokhlov, N.E.; Gerevenkov, P.I.; Shelukhin, L.A.; Azovtsev, A.V.; Pertsev, N.A.; Wang, M.; Rushforth, A.W.; Scherbakov, A.V.; Kalashnikova, A.M. Optical Excitation of Propagating Magnetostatic Waves in an Epitaxial Gallenol Film by Ultrafast Magnetic Anisotropy Change. *Phys. Rev. Appl.* **2019**, *12*, 044044. [[CrossRef](#)]

-
29. Mizukami, S.; Sajitha, E.P.; Watanabe, D.; Wu, F.; Miyazaki, T.; Naganuma, H.; Oogane, M.; Ando, Y. Gilbert damping in perpendicularly magnetized Pt/Co/Pt films investigated by all-optical pump-probe technique. *Appl. Phys. Lett.* **2010**, *96*, 152502. [[CrossRef](#)]
 30. Widom, A.; Vittoria, C.; Yoon, S.D. Gilbert ferromagnetic damping theory and the fluctuation-dissipation theorem. *J. Appl. Phys.* **2010**, *108*, 073924. [[CrossRef](#)]
 31. Ovcharenko, S.; Gaponov, M.; Klimov, A.; Tiercelin, N.; Pernod, P.; Mishina, E.; Sigov, A.; Preobrazhensky, V. Ultrafast manipulation of magnetic anisotropy in a uniaxial intermetallic heterostructure TbCo₂ /FeCo. *J. Phys. D Appl. Phys.* **2022**, *55*, 175001. [[CrossRef](#)]